Non-local equilibrium continuum modeling of partially saturated drying porous media: Comparison with pore network simulations

Faeez Ahmad, Marouane Talbi, Marc Prat, Evangelos Tsotsas, Abdolreza Kharaghani

Non-local equilibrium continuum modeling of partially saturated drying porous media: Comparison with pore network simulations

Faeez Ahmad[1], Marouane Talbi[2], Marc Prat[2], Evangelos Tsotsas[1], Abdolreza Kharaghani[1]

[1]Otto-von-Guericke University Magdeburg, Universitaetsplatz 2, 39106 Magdeburg, Germany

[2]INPT, UPS, IMFT (Institut de Mécanique des Fluides de Toulouse), Université de Toulouse, Allée Camille Soula, F-31400 Toulouse, France and CNRS, IMFT, F-31400 Toulouse, France

Corresponding author: mprat@imft.fr (M. Prat)

Abstract

A two-equation continuum model is developed to simulate the mass transfer in drying porous media. The main goal is to capture the so called non-equilibrium effect. To this end, we operate in a regime where the liquid phase is immobile so that non-equilibrium mass exchange between liquid and vapor phase dominates. The formulation of the model relies on an upscaling technique. This notably permits to formulate the non-local equilibrium phase change term on a firmer basis. The upscaling also indicates that there is no reason to consider an enhancement factor in the vapor diffusion model. The macroscopic model parameters are determined from pore network drying simulations. The same simulations are also used as a reference to compare with the predictions of the non-local equilibrium continuum model. The solution of the two-equation continuum model proves that this model simulates the non-local equilibrium effect with reasonable accuracy. Also, the simulations indicate that the non-local equilibrium effect is especially significant at the porous medium surface.

Keywords: upscaling, non-equilibrium effect, specific interfacial area, pore network simulations

1. Introduction

The evaporation from porous media is a key natural and industrial process. The modeling of drying porous media has been a subject of research for decades. Heat and mass transfer during the two stages of drying is more commonly described using the concept of continuum

modeling (CM). A presentation of the most popular continuum model in this context can be found in (Whitaker, 1977), where heat and mass transfer during evaporation in porous medium was extensively modeled in the framework of the volume averaging method. This widely used CM combines the equations for the liquid flow and the vapor flow into a single equation under the assumption of local equilibrium (LE) between the vapor and the liquid phases. However, this assumption has been questioned (Bénet and Jouanna, 1982). It was argued that the equilibrium characteristic time $t_{eq} \approx L^2/D_v$, where L is a characteristic length of the porous medium and D_v is the vapor diffusivity, was too long for the local equilibrium condition to be satisfied during drying. This leads to a different class of models where the liquid flow equation and the vapor flow equation are not merged into a single equation and both contain a non-equilibrium phase change term. One can refer, for instance, to (Li et al., 2019) for a presentation of the NLE CM together with the more classical LE CM model. The NLE effect is considered to be especially significant in hygroscopic materials (see, e.g., Bénet and Jouanna 1982; Bénet et al., 2009; Ouedraogo et al., 2013). However, in capillary porous materials, in which pore liquid is spatially allocated by capillary effects and thus adsorption phenomena are negligible, the NLE effect has been treated as a seemingly less important issue. However, the pore network model (PNM) simulations reported in (Attari Moghaddam et al., 2017) clearly indicate that the NLE effect is also present during the drying of capillary porous media. As a consequence of the NLE effect, it was shown that the saturation profiles computed from the pore network simulations could not be simulated with the classical LE model using a single set of macroscopic parameters (Vorhauer et al., 2010). Also, the drying kinetics could not be simulated over the complete drying process using the classical one-equation CM model (Attari Moghaddam et al., 2017). The conclusion was therefore that a NLE CM formulation should be considered not only for hygroscopic materials as suggested by Bénet and co-workers but also for capillary porous media. The present work is a step in this direction.

The methodology used in this work is the same as in (Attari Moghaddam et al., 2017). PNM simulations are used for generating reference data, such as saturation profiles and drying kinetics. Then, the NLE CM is tested against the volume averaged PNM data. Compared to (Attari Moghaddam et al., 2017), the new feature is that a NLE continuum model is considered. Hints on the formulation of the NLE phase change term in this model are obtained using the volume averaging method. Also, as in previous work on the NLE effect, i.e. (Ouedraogo et al., 2013), we focus on the conditions of low initial saturation. In our case,

this corresponds to a situation where the liquid phase is formed by a set of disconnected small clusters. This enables us to concentrate on a situation where the vapor transport is a dominant mechanism. Similarly to (Attari Moghaddam et al., 2017), evaporation is controlled by mass transfer and the temperature variation is negligible.

The paper is organized as follows: In Section 2, the formulation of the two-equation CM is described in detail. The pore network drying algorithm is explained in Section 3. The method for computation of macroscopic effective parameters is described in Section 4. Results of PNM drying simulations are presented in Section 5, and macroscopic parameters are discussed in Section 6. NLE CM simulations are compared to PNM drying reference data in Section 7, with some further discussion in Section 8. Finally, Section 9 summarizes the key results and outlines possible future research directions.

2. Continuum model formulation

As discussed in several previous works, i.e. (Li et al., 2019; Ouedraogo et al., 2013) and references therein, the NLE continuum model can be expressed as a system of two coupled equations, one for the liquid flow and one for the vapor flow. When the liquid phase is formed by small disconnected clusters, there is no macroscopic flow in the liquid phase and the model can be simplified. Under these circumstances, it can be expressed as

$$\varepsilon \frac{\partial (1-S) P_v}{\partial t} = \nabla . \left(\varepsilon (1-S) D_{eff} \nabla P_v \right) + \frac{\tilde{R} T}{\widetilde{M}_v} \dot{m} \tag{1}$$

for the vapor flow and

$$\varepsilon \rho_l \frac{\partial S}{\partial t} \approx -\dot{m} \tag{2}$$

for the liquid phase (considered to be immobile). In Eqs. (1) and (2), ε, t, D_{eff}, S, ρ_l and P_v denote the porosity, time, macroscopic vapor diffusion coefficient, liquid saturation, water density and water vapor partial pressure, respectively. $\widetilde{M}_v$, $\tilde{R}$ and T represent the molar mass of water, universal gas constant, and temperature; $\dot{m}$ is the phase change rate between the liquid and vapor phases. The latter is also referred to as the NLE phase change term. Different formulations are proposed for $\dot{m}$ in the literature. In the works of Bénet and co-workers, i.e. (Ouedraogo et al., 2013) and references therein, $\dot{m} = \beta \frac{\tilde{R} T}{\widetilde{M}_v} ln \left(\frac{P_v}{P_{v,eq}} \right)$ where $P_{v,eq}$ is the equilibrium vapor pressure and β is a phenomenological coefficient which notably depends on the porous medium microstructure. In (Li et al., 2019), this term was expressed as

$\dot{m} = b\varepsilon(S - S_{res})\frac{\tilde{R}T}{\tilde{M}_v}\left(P_{v,eq} - P_v\right)$ where b is a coefficient and S_{res} is the residual water content. The same expression was used in (Pujol et al., 2011) with $S_{res} = 0$. In order to clarify the formulation of $\dot{m}$ a derivation using the volume averaging method (Whitaker, 2013) is presented in Appendix A taking advantage of the mathematical analogy with the problem of diffusion with heterogeneous reaction presented in (Whitaker, 2013). This leads to express the NLE phase change term as

$$\dot{m} \approx -a_{gl}\frac{\widetilde{M}_v}{\tilde{R}T}k\left(P_{v,eq} - P_v\right), \tag{3}$$

where a_{gl} is the specific interfacial area between liquid and vapor phases and k is a coefficient. In our case $P_{v,eq}$ is equivalent to $P_{v,sat}$. $P_{v,sat}$ is the saturation water vapor partial pressure since adsorption phenomena are not considered in the PNM simulations on the ground that they are negligible in capillary porous media. Another noticeable outcome from the derivation presented in Appendix A is that the effective coefficient D_{eff} can be computed as if the liquid was simply acting as a solid obstacle to vapor diffusion. In other terms and contrary to the consideration on vapor diffusion in drying by (Philip and De Vries, 1957) the derivation does not suggest that an enhancement effect should be considered in the determination of D_{eff} as a result of phase change within the representative elementary volume. One can refer, for instance, to (Plumb et al., 1999) for more details on the vapor diffusion enhancement factor.

To simulate the drying problem with the NLE CM (Eqs. (1-3)), three macroscopic coefficients must be determined, namely a_{gl}, D_{eff} and k, noting that a_{gl} and D_{eff} are functions of saturation. The method to determine these coefficients is presented in Section 4. Then, initial and boundary conditions must be specified. The pore network is initially saturated with liquid and supposed to be at equilibrium. Thus $P_v = P_{v,sat}$ throughout the computational domain at $t = 0$. The initial liquid phase saturation is computed by volume averaging the initial liquid water distribution in the pore network.

The two-equation CM is solved in 1D by discretizing the computational domain by using finite volume method. At the bottom of the domain, a zero-flux boundary condition is applied, whereas at the evaporative surface the specific evaporation rate is computed by the following equation:

$$\varepsilon(1 - S)\frac{\widetilde{M}_v}{\tilde{R}\,T}D_{eff}\nabla P_v.\,\mathbf{n} = -\frac{\widetilde{M}_v}{\tilde{R}\,T}D_{va}\frac{P_{v,surf} - P_{v,\infty}}{L_{bl}}, \tag{4}$$

where D_{va}, L_{bl}, $\mathbf{n}$, $P_{v,surf}$ and $P_{v,\infty}$ denote the water vapor molecular diffusion coefficient, external boundary layer thickness, unit normal vector directed toward the external boundary layer, vapor pressure of the surface volume element and vapor pressure in the bulk air, respectively. The formulation of the boundary conditions at the evaporative surface is actually not that obvious with the two-equation NLE CM model since both liquid and vapor pores can be present at the surface. The question thus arises as to how the external evaporation flux should be split into a contribution from the evaporation of the surface liquid pores and a contribution from surface pores occupied by the gas phase. However, the consideration of an immobile liquid phase, i.e. Eq. (2), simplifies the modeling of the exchange at the evaporative surface since no boundary condition is actually needed in conjunction with Eq. (2). Only boundary conditions for Eq. (1) are needed.

3. Pore network model algorithm

In our pore network model, the pore space is conceptualized by cylindrical tubes referred to as throats. The connectivity between these throats is provided by pore nodes which serve only as computational points and do not carry any volume. The radii of the cylindrical throats follow a normal distribution which is based on mean radius and standard deviation. The lateral edges are connected to each other (periodic boundary condition). The network of pore nodes extends outside the pore network domain into the discretized boundary layer. External mass transport occurs through this diffusive boundary layer from the evaporating meniscus throats at ambient conditions. In this work, pore network simulations are carried out in three-dimensional space.

In the pore network model, we operate in the special regime where the liquid phase is immobile. In a capillary porous medium, this special regime can be created by considering an initial liquid phase structure which consists of isolated liquid clusters (see Fig. 1). These liquid clusters are minimally sized and are located randomly inside the network. While capillary pumping is considered, we neglect the influence of viscosity in the liquid phase. Moreover, the discontinuity of the liquid phase effectively means that there is no mass transport through the network in liquid phase, eliminating the need to compute liquid pressure field. Hence mass transport essentially occurs only through water vapor diffusion in the gas phase. This means that the volume-less pores are used to compute only the gas phase vapor partial pressure through Stefan's flow based on

$$J_{v,k} = \pi r_t^2 \frac{\widetilde{M}_v}{\tilde{R}\, T\, L_t} P_{atm} D_{va} ln\left(\frac{P_{v,i} - P_{atm}}{P_{v,j} - P_{atm}}\right). \quad (5)$$

At each pore node, mass balance for vapor flux is applied, enabling us to obtain a system of equations based on linearized version of Eq. (5), which is then numerically solved to obtain the vapor pressure field. This means that we obtain values of partial vapor pressure at each pore node present inside and outside (boundary layer) the network. The discretization of the drying process is associated with the time for emptying of one meniscus throat, during which the vapor flow is assumed to be quasi-steady. For the next time step, the vapor pressure field is calculated based on the updated boundary conditions.

As the drying process goes on, the liquid clusters shrink and split into isolated menisci. The calculation of vapor transport is considered independently for each cluster. To this end, it is essential to label the liquid clusters. This is achieved by employing a variant of the Hoshen-Kopelman algorithm (Metzger et al., 2006). The drying process goes on until the liquid in the network has been entirely evaporated. We assume that the porous medium is non-hygroscopic; without adsorption a completely unsaturated network is achieved at the end of the drying process. Furthermore, secondary capillary structures (liquid films and rings) are not considered in the model. In addition to this, due to slow drying (at ambient conditions), the process is assumed to be isothermal, therefore we do not consider the role of viscosity for gas transport and assume a constant pressure at all pore nodes. For the details beyond the present brief discussion of the fundamentals of PNM for drying, the reader may refer to (Prat, 2002; Metzger et al., 2007; Prat, 2011).

Fig.1: A 2D representation of 50×50 pore network in which the liquid phase (shown in blue) is distributed as isolated clusters. The gas and solid phases are represented in white and grey, respectively. Note that for our discrete simulations 3D pore networks are used.

4. Method for computation of CM parameters

Macroscopic parameters can be determined from dedicated PNM simulations, e.g. (Øren et al., 1998; Blunt et al., 2001). Most of the literature in this regard pertains to the drainage process, and the focus is on relative and absolute permeabilities and capillary pressure curve. The use of PNM for drying porous media (Nowicki et al., 1992; Attari Moghaddam et al., 2017) has also been done along similar lines with the addition of computation of vapor diffusivity. This requires developing specific computations over a representative elementary volume (REV). In what follows, we proceed somewhat differently and make use of a method

inspired from the method used to determine the moisture transport coefficient from drying experimental results in previous works. Typically, in these experiments, transient saturation profiles were determined for a given set of conditions (e.g. Schoeber, 1976; Marchand and Kumaran, 1994; Pel et al., 1996; Gomez et al., 2007). Subsequently these saturation profiles were used to compute moisture transport coefficients. In our case, the saturation profiles are obtained from volume averaging of the appropriate PNM drying simulation data and we also use the volume averaged vapor pressure profiles.

The macroscopic parameters determined from PNM drying simulations are effective vapor diffusivity and specific interfacial area. As mass transport is in the gas phase only (immobile liquid phase), we do not compute liquid diffusivity. The dependency of macroscopic effective vapor diffusivity and specific interfacial area on local saturation is determined using the data obtained from PNM drying simulations. For our PNM, the computation is carried out on two levels: on the scale of pore throats, we compute the liquid saturation and on the scale of volume-less pore nodes we compute partial vapor pressure.

The data at the pore scale is transformed into macroscopic scale by dividing the three-dimensional pore network into horizontal slices of thickness Δz – an exemplary 3D pore network is illustrated in Fig. 2. Here one slice is the macroscopic averaging volume over which local saturation and vapor pressure are computed. As shown in Fig. 2, we characterize a slice such that it consists of pore-nodes which lie on the side of top bounding plane of the slice, horizontal throats directly connected to these pore-nodes and the neighbor vertical throats that are directed towards the bottom. The local saturation of the slice is computed by calculating the ratio of liquid volume in the throats contained in the slice to the total volume of throats in the slice. For the computation of local vapor pressure in the slice, we compute the arithmetic mean of the vapor pressures of the pores contained inside the slice. The characterization of the surface slice is different from other slices due to the fact that in PNM the pore-nodes in surface plane do not have any directly connected horizontal throats.

The vapor flux j_v through all vertical throats in a slice is computed using the vapor pressure of pore nodes through Eq. (5) and summed up to give the total vapor flux passing through a slice. This total flux is then divided by the cross-section area of the plane (as illustrated in Fig. 2 by A_{plane}) to provide j_v which is then used to compute D_{eff} from the flux between two slices using

$$D_{eff} = -\frac{\tilde{R}\,T}{\widetilde{M}_v}\frac{j_v}{\varepsilon(1-S)\,\frac{\partial P_v}{\partial z}}. \quad (6)$$

Apart from this, in order to neglect the local transport in liquid phase, the size of liquid clusters is kept small in a way that they do not span over a slice. Hence, interslice liquid transport is avoided by restricting the cluster size. Additionally, we compute the specific interfacial area a_{gl} by summing up cross-section area of interfacial throats belonging to a slice and divide it by the total macroscopic volume of that slice. It should be noted that the interfacial area is measured at the meniscus level and not at the pore-node, meaning that one gas pore can have several interfacial throats connected to it.

Fig. 2: A sample pore network illustration with evaporative surface on top and a slice (local averaging volume) cut perpendicular to z direction from the pore network consisting of one row of nodes (connected to top side of vertical throats) for computation of vapor pressure. The throats filled with liquid are represented in blue and gas-filled throats in gray. A_{plane} represents network cross-section area and Δz represents the thickness of slice. The computational nodes in the external boundary layer on top of the network are not visible here.

5. PNM drying simulation results

The input parameters that specify the structure and physical conditions for PNM drying simulations are listed in Table 1. To minimize the influence of randomness in throat size distribution and initial liquid phase structure on the macroscopic parameters, we carried out 45 simulations each with different realization of throat size distribution and initial liquid phase structure (location of liquid clusters). All the results shown in this section are averaged over these 45 simulations (unless stated otherwise). As the liquid phase is discontinuous and the size of clusters is very small, the viscosity of liquid phase becomes irrelevant. We operate in the capillary-dominated regime as far as the evolution of the liquid phase is concerned. Mass transport through the network is purely controlled by diffusion in the gas phase. To produce the initial liquid phase structure with discontinuous liquid phase, we can have an arbitrary amount of liquid in the network. We choose an arbitrary initial network saturation of 0.26 for the PNM drying simulations and the subsequent CM solution.

Table 1: Structural and physical parameters for PNM simulations.

5.1 Drying kinetics and saturation profiles

240 The evolution of overall network saturation S_{net} with time and the change in normalized total
241 evaporation rate with respect to S_{net} are shown in Fig. 3. The evaporation rate drops sharply
242 as the surface water evaporates, followed by a consistent decrease in evaporation rate.

243 Fig. 3: Variation of network saturation S_{net} with drying time (left) and normalized evaporation
244 rate with respect to S_{net} (right).

245 Compared to the classical drying kinetics for capillary porous media, no constant rate period
246 (CRP) is observed. This behavior is in accordance with the initial condition imposed in our
247 simulations for the liquid phase distribution. As illustrated in Fig. 4, the drying situation is
248 characterized by a traveling drying front where the saturation varies abruptly from the initial
249 saturation to zero. The saturation plotted in Fig. 4 and denoted by S_{loc} corresponds to the
250 saturation determined in each slice of the network (as defined in Sec. 4). Referring to the
251 drying kinetics classical description in three periods (van Brakel, 1980), our case is close to
252 the last period, referred to as the receding front period (RFP) where a dry zone develops into
253 the porous medium from the surface (Pel et al., 1996). As will be discussed later, the
254 dynamics of the drying front, i.e. how the position of the front scales with the elapsed time, is
255 however different in our simulations.

256 Fig. 4: Saturation profiles (left) and normalized vapor pressure profiles (right) obtained from
257 two-equation CM (blue dashed lines) and PNM (black solid lines). CM results are plotted for
258 times that correspond to S_{net} of 95, 90, 80, 60, 40, 20 and 10 % of $S_{net,ini}$ for PNM simulation
259 results. The outer surface lies at $z/H = 1$ in both figures.

260 ## 5.2 Non-local equilibrium effect

261 The ratio of P_v to $P_{v,sat}$ as a function of both local saturation and network saturation
262 characterizing the non-local equilibrium is obtained from PNM simulations and illustrated in
263 Fig. 4. Based on continuity of vapor flow, the closer a pore is to the boundary layer, the lower
264 is the vapor pressure of the pore. Hence, when the drying front is on the surface, the vapor
265 pores constituting the surface slice exhibit the lowest vapor pressure of any slice. As the
266 drying front recedes into the network, the NLE effect decreases because the distance from the
267 boundary layer increases. As shown in Fig. 5, the NLE effect increases abruptly, i.e. the ratio
268 of P_v to $P_{v,sat}$ decreases significantly, for very low saturations ($S_{loc} < 0.03$ in Fig. 5); this
269 corresponds to the drying front where the saturation varies sharply over a small distance (see
270 the saturation profiles in Fig. 4).

Fig. 5: Averaged value of NLE indicator as a function of local saturation (S_{loc}) for different intervals of network saturation (S_{net}).

6. Macroscopic parameters from PNM simulations

6.1 Computation of water vapor diffusivity

Figure 6 shows the variation of the ratio of D_{eff} to D_{eff}^* with respect to local saturation obtained from PNM drying simulations. D_{eff}^* is D_{eff} $(S_{loc}= 0)$, i.e. the effective vapor diffusivity for a completely dry network. The local saturation here is computed as an arithmetic mean of saturation of the two successive local averaging volumes between which the vapor transfer occurs. As expected the value of D_{eff} is highest when the vapor flux faces no resistance from the presence of liquid phase, i.e. when D_{eff} is equal to D_{eff}^*.

Fig. 6: Ratio of D_{eff} to D_{eff}^* with respect to averaged local saturation. The black solid line represents the fitted profile through the discrete data points shown by blue symbols.

We observe an initial increase in D_{eff} with decreasing S_{loc} followed by an intermediate period of approximately constant value and then a sharp increase in D_{eff} until zero local saturation has been reached. The plateau for the intermediate local saturation range has generally not been observed in previous works, i.e. (Pel et al., 1996), in which the vapor diffusivity decreases continually with increasing saturation. The difference is that here we start from a different liquid phase distribution where the liquid phase is distributed in small isolated clusters. The results shown in Fig. 6 indicate that the tortuosity of the gas phase does not vary significantly over the intermediate range of saturations in our case.

6.2 Computation of specific interfacial area

Using PNM drying simulations, we compute the specific interfacial area a_{gl} i.e. the sum of interfacial area of the interfacial throats contained within a local averaging slice divided by the macroscopic volume of a local averaging slice. Initially each local slice occupies a moderate value of a_{gl} of around 150 m^2/m^3 as illustrated in Fig. 7. As the drying process begins, the uniformly distributed liquid clusters in the evaporating slices split into isolated meniscus throats. As a consequence of the small size of the liquid clusters, the total interfacial area of the resulting isolated menisci is greater than that of the parent cluster. This phenomenon is the cause of the initial increase in a_{gl} until a peak is reached at around $S_{loc} \approx 0.16$. Upon further drying, the rate of local production of interfacial area is overcome by the rate of removal of liquid throats, resulting in consistent decrease of a_{gl} with local saturation.

Fig. 7: Specific interfacial area a_{gl} as a function of local saturation S_{loc}. The data points are averaged over finite local saturation intervals. The black solid line is a fitted function of a_{gl} out of the discrete data points (blue symbols).

7. CM simulation results compared with PNM results

The macroscopic effective vapor diffusivity D_{eff} and specific interfacial area a_{gl} (indicated by fitted functions illustrated in Fig. 6 and Fig. 7, respectively) obtained from PNM drying simulations are used to solve the two-equation CM (Eqs. (1) and (2)). The only missing parameter is the mass exchange coefficient k. The latter is used as a fitting parameter. Figure 4 shows the saturation profiles and normalized vapor pressure profiles obtained from the solution of two-equation CM at seven distinct times compared with corresponding PNM simulation results for the k value of 0.05 m/s. The comparison of saturation and vapor pressure profiles indicates that the two-equation CM reproduces the profiles with good accuracy.

Figure 8 shows the evaporation rate obtained by the NLE CM compared with the evaporation rate obtained from corresponding PNM simulations results. The initial saturation assigned to the discretized finite volume elements of the CM is 0.26 and the corresponding initial vapor partial pressure is given as $P_{v,sat}$ for all slices. The assigned initial condition for P_v is the reason for the higher initial value of evaporation rate of CM simulation compared to the corresponding initial value of PNM simulation (as can be seen in Fig. 8). However, the CM adjusts the value of P_v of surface volume element (and the surrounding elements) very quickly (in the first second of drying time), therefore this discrepancy in the initial evaporation rate does not affect the solution.

Fig. 8: Comparison of evaporation rates obtained from PNM drying simulations and that predicted by two-equation CM.

Additionally, we can analyze the ability of two-equation CM to reproduce the NLE effect. This is illustrated in Fig. 9. In doing so, we illustrate the comparison of NLE effect reproduced by two-equation CM simulation and the corresponding PNM simulation results for varying ranges of network saturation. Based on the convergence of saturation profiles, vapor pressure profiles, total evaporation rate and the NLE effect, it can be said that the two-equation NLE CM produces good results.

Fig. 9: NLE effect obtained from PNM drying simulation and solution of two-equation NLE CM for varying ranges of S_{net}. The solid lines represent the PNM results and the dashed lines represent NLE CM simulation results.

8. Discussion

8.1 NLE CM simulation results compared with LE front model

Since the drying front is quite sharp, the particular situation considered in this work is classically analyzed using a traveling front model under the assumption of local equilibrium, $P_v = P_{v,sat}$ at the front, i.e. regardless of the degree of local saturation within the front region. Under the classical quasi-steady approximation for the water vapor transport, the mass balance at the front is expressed as

$$j_v = \frac{\widetilde{M}_v}{\tilde{R}\,T} D^*_{eff} \frac{P_{v,sat} - P_{v,surf}}{z_f} = \varepsilon \rho_l S_{net,ini} \frac{dz_f}{dt}, \tag{7}$$

where z_f denotes the position of the front (distance from the surface) and $S_{net,ini}$ the initial network saturation. Combining Eq. (7) with the right-hand side of Eq. (4), i.e. $j_v = \frac{\widetilde{M}_v}{\tilde{R}\,T} D_{va} \frac{P_{v,surf} - P_{v,\infty}}{L_{bl}}$, leads to an ordinary differential equation which can be solved analytically. This leads to a solution where the front position typically scales with the square root of time, i.e. $z_f \propto \sqrt{t}$. In what follows, the LE front model is referred to as the LE CM.

Figure 10 shows the drying front position predicted by LE CM compared with that obtained from PNM drying simulations and the two-equation NLE CM. It can be seen that the NLE CM reproduces the drying front position very well. On the other hand, the drying front position predicted by the LE CM is shifted by a certain amount in relation to that obtained from PNM drying simulations.

Fig. 10: (Left) Variation of normalized drying front position ξ with respect to time. (Right) Total evaporation rate per unit area with respect to network saturation. Both figures present a comparison of results of PNM drying simulations presented in Sec. 5 and the corresponding NLE CM and LE CM simulation results.

The corresponding comparison of evaporation rate however reveals that the evaporation rates from PNM, LE CM and NLE CM do not differ significantly in the course of the process. Though it should be noted that in NLE CM, the initial evaporation rate drops instantaneously to the correct value corresponding to the initial evaporation rate of the PNM results. On the

other hand, in the LE CM the initially overestimated drying rate affects the overall drying time as well as the drying front position as can be seen in the comparison of drying front position with respect to time (Fig. 10). Consistently with the NLE curves in Figs. 5 and 9, the impact of the NLE effect is only important at the beginning of the drying process when the drying front is at the surface or very close to it. Nevertheless, the impact of the error at the beginning associated with the LE CM affects the position of the drying front as illustrated in Fig. 10.

8.2 On the specific interfacial area

A key parameter introduced in the two-equation NLE CM is the specific interfacial area a_{gl}. It is a measure of liquid or gas phase tortuosity in a two-phase flow situation and is considered very important especially in the modeling of drainage process inside a porous medium. The general shape of the a_{gl} curve as illustrated in Fig. 7 is consistent with several previous results from the literature. For example in (Joekar-Niasar et al., 2008; Joekar-Niasar et al., 2010) we see a similar non-monotonic polynomial relationship between saturation and specific interfacial area. For comparison with experimental results we can refer to (Culligan et al., 2006) where drainage experiments are performed on glass beads that have a_{gl} values in similar ranges as the ones shown Fig. 7, i.e. from 0 to 0.23 mm^{-1}. More recently, the work done by (Wang et al., 2019) has also qualitatively validated the specific interfacial area function.

While operating in the limiting regime of immobile liquid phase, we could work with different degrees of initial network saturation $S_{net,ini}$. In order to illustrate the effect of degree of initial network saturation on a_{gl}, we arbitrarily selected 4 different values of initial network saturation and performed 15 simulations for each value of $S_{net,ini}$, each with a different realization of throat size distribution and location of liquid clusters. In Fig. 11 the averaged a_{gl} obtained from the various realizations for each case of $S_{net,ini}$ is illustrated. For all $S_{net,ini}$, we see a qualitatively similar trend, i.e. an initial increase in a_{gl} followed by a consistent decrease with decreasing local saturation. When the results of different $S_{net,ini}$ are compared quantitatively, it is observed that overall the a_{gl} values decrease with decrease in $S_{net,ini}$ for their respective local saturation values. This is owed to the fact that while operating in the limiting regime of immobile liquid phase, the total interfacial area per unit volume is higher when there are more liquid throats per unit volume.

Fig. 11: Specific interfacial area a_{gl} as a function of local saturation S_{loc} simulated with varying degree of $S_{net,ini}$. Each of the four functions presented here is the result of averaging of 15 simulations, each with different realizations of the randomly generated throat size distribution and the liquid structure.

This dependency of a_{gl} on the initial saturation illustrated in Fig. 11 can be related to some considerations about a_{gl} in two-phase flow modeling where the specific interfacial area is modeled by a dedicated conservation equation, e.g. (Hassanizadeh and Gray, 1990; Hassanizadeh and Gray, 1993). As shown in (Joekar-Niasar et al., 2008) the classical capillary pressure-saturation relationship is incomplete without the consideration of specific interfacial area. Considering the interfacial area is a vital step to circumvent the hysteresis in capillary-pressure and relative permeability and saturation relationships. Here, the results shown in Fig. 11 can be seen as another illustration of the fact that the saturation alone is not sufficient to derive the macroscopic parameters, since the parametrization of the NLE phase change term in the NLE CM, i.e. Eq. (3), in fact depends on the initial network saturation $S_{net,ini}$ through the dependency of a_{gl} on $S_{net,ini}$ illustrated in Fig.11.

Also, it can be noted from Fig. 11, that a_{gl} varies roughly linearly with local saturation for sufficiently low local saturation values. Then, it can be observed that our expression of the phase change term, i.e. Eq. (3), is consistent with the expression used in (Li et al., 2019; Pujol et al., 2011), namely $\dot{m} = b\varepsilon(S - S_{res})\frac{\tilde{R}T}{\tilde{M}_v}\left(P_{v,eq} - P_v\right)$ in this range of saturation, which is the most critical for the NLE effect according to Figs. 5 and 7.

8.3 On the receding front period

The saturation evolution depicted in Fig. 4 resembles the evolution in the receding front period (RFP) reported in several previous works where the profiles were determined experimentally, e.g. (Pel et al., 1996, 2002). However, there is an important difference. In the experimental results presented in (Pel et al., 1996, 2002), the position of the front scales linearly with time, see also (Lockington et al., 2003), whereas in our case the front position scales with the square root of time (Fig. 10). The difference is due to the impact of the viscous effects, which are completely neglected in our simulations since the liquid phase is disconnected. In the experiments, the liquid is still connected, i.e. percolating between the front and the sample bottom, and the receding of the front results from the balance between the evaporation rate and the liquid flow at the front. In other words, the situation considered in our simulations rather corresponds to the special case where viscous effects in the liquid

423 can be completely neglected compared to capillary effects. In this limiting case, the liquid
424 phase is disrupted during the receding front period as shown for instance in (Le Bray and
425 Prat, 1999).

426 9. Conclusions

427 In this study, a non-local equilibrium (NLE) continuum model (CM) of drying was studied by
428 comparison with pore network simulations for the case where the liquid phase is initially
429 distributed in the form of small disconnected clusters. The CM was derived with the help of
430 the volume averaging method. This led to the introduction of the specific interfacial area in
431 the formulation of the NLE phase change term. Also, the upscaling suggests that there is no
432 particular reason for introducing an enhancement factor in the vapor diffusion model.

433 Pore network model (PNM) simulations indicated that an NLE effect should be expected not
434 only for hygroscopic materials, as suggested in several previous works (Bénet and Jouanna,
435 1982; Bénet et al., 2009; Ouedraogo et al., 13), but also in the case of capillary porous
436 materials. The study also indicates that the NLE effect is particularly marked at the surface.
437 This should be taken into account in the modeling of the coupling between the internal
438 transfer, i.e. inside the porous medium, and the external transfer, i.e. within the external
439 boundary layer. In other words, the study suggests that a significant improvement in the
440 modeling of the drying process by means of continuum models can be expected from the
441 consideration of the NLE effect in the porous medium evaporative surface region.

442 The NLE CM led to a good agreement with the PNM drying simulations in both the
443 saturation profiles and the drying kinetics. However, for the considered situation, the NLE
444 CM leads to only slightly better results than the simpler LE front model. Nevertheless, the
445 NLE CM is much more conceptually consistent with the drying PNM simulations which
446 clearly indicate an NLE effect. The next step will be to test the NLE CM over a full drying,
447 that is when the porous medium is fully saturated initially. This will imply to consider the so
448 called constant rate period (CRP) and, the falling rate period (FRP) (van Brakel, 1980) where
449 a significant NLE effect is expected, notably at the evaporative surface. We then expect that
450 the NLE CM will be not only conceptually better but also quantitatively better than the LE
451 CM.

452 Like other macroscopic parameters, such as the capillary pressure curve or the relative
453 permeabilities, the parameters of the drying model can be determined from PNM simulations.
454 However, it should be noted that we have determined these parameters from the PNM

simulations of the drying process in a manner somewhat similar to the determination of moisture diffusivity from drying experiments, i.e. (Pel et al., 1996). Within the framework of PNM, it is more classical to determine the parameters using dedicated algorithms. We mean here, for instance, a specific algorithm to determine the permeability curve or the capillary pressure curve, see, e.g., (Blunt et al., 2001) and references therein. In this respect, it would be interesting to develop a specific algorithm for determining the mass transfer coefficient k of the NLE phase change term, see Eq. (3), so as to study the impact of microstructure on this coefficient. In the framework of the volume averaging method, this means developing the closure problem enabling one to compute k.

Acknowledgement

This work was financed within the frame of our joint project "Drycap" funded by DFG (project TS28/10-1) and GIP ANR (project 16-CE92-0030-01).

Appendix A

In this appendix we present the details of derivation of the two-equation CM comprising of transport equations for liquid and vapor phases. Starting point is the pore scale description of vapor transport in the domain occupied by the gas phase in the porous medium

$$\frac{\partial \rho_v}{\partial t} = \nabla.(D_v \nabla \rho_v), \tag{A1}$$

where ρ_v and D_v denote the vapor density and vapor diffusion coefficient, respectively. The boundary condition at the solid-gas interface can be expressed as

$$-D_v \nabla \rho_v . \mathbf{n}_{gs} = 0, \tag{A2}$$

where $\mathbf{n}_{gs}$ is the unit vector in the direction perpendicular to the solid-gas interface. At the liquid-gas interface (A_{gl}), we make use of the Hertz-Knudsen-Schrage (HKS) equation (Schrage, 1953) and express the boundary condition as

$$-D_v \nabla \rho_v . \mathbf{n}_{gl} = -\frac{2\sigma}{2-\sigma}\sqrt{\frac{\widetilde{M}_v}{2\pi k_B}}\left(\frac{P_{v,sat}}{\sqrt{T_l}} - \frac{P_v}{\sqrt{T_g}}\right), \tag{A3}$$

where $\mathbf{n}_{gl}$, $\widetilde{M}_v$, k_B, σ, T_g, T_l denote the unit normal vector perpendicular to the gas-liquid interface, molar mass of water vapor, Boltzmann constant, accommodation coefficient, gas

478 temperature and liquid surface temperature, respectively. Assuming $T_l = T_g$ and using T to
479 represent the temperature, Eq. (A3) can be expressed as

$$-D_v \nabla \rho_v . \mathbf{n}_{gl} = -\frac{2\sigma}{2-\sigma}\sqrt{\frac{\widetilde{M}_v}{2\pi k_B T}}\left(P_{v,sat} - P_v\right). \tag{A4}$$

480

481 Using ideal gas law, we can express Eq. (A1) in terms of P_v as

$$\frac{\partial P_v}{\partial t} = \nabla . (D_v \nabla P_v). \tag{A5}$$

482 Similarly expressing Eqs. (A2) and (A4) in terms of P_v

$$-D_v \nabla P_v . \mathbf{n}_{gs} = 0, \tag{A6}$$

483

$$-D_v \nabla P_v . \mathbf{n}_{gl} = -k\left(P_{v,sat} - P_v\right), \tag{A7}$$

484 where

$$k = \frac{2\sigma}{2-\sigma}\sqrt{\frac{T\tilde{R}^2}{2\pi k_B \widetilde{M}_v}}. \tag{A8}$$

485 Here with the intention to re-formulate the vapor transport equations at the pore-scale, we
486 define a new variable P_v^* as

$$P_v^* = P_{v,sat} - P_v. \tag{A9}$$

487 Using Eq. (A7) we re-formulate the problem of vapor transport at the pore-scale in terms of
488 P_v^* and express Eq. (A5) as

$$\frac{\partial P_v^*}{\partial t} = \nabla . (D_v \nabla P_v^*). \tag{A10}$$

489 Similarly, we can express Eqs. (A6) and (A7) as

$$-D_v \nabla P_v^* . \mathbf{n}_{gs} = 0, \tag{A11}$$

490

$$-D_v \nabla P_v^* . \mathbf{n}_{gl} = k P_v^* . \tag{A12}$$

Invoking the advantage of the analogy between the problem of diffusion and heterogeneous reaction presented in (Whitaker, 2013) and using the volume averaging method (Whitaker, 2013), we upscale the problem leading to the volume transport macroscopic equation

$$\varepsilon(1-S)\frac{\partial P_v^*}{\partial t} = \nabla . \left(\varepsilon(1-S) D_{eff} \nabla P_v^*\right) + \nabla . (\mathbf{u} P_v^*) - a_{gl} k P_v^*, \tag{A13}$$

where we use the same notation for the volume averaged partial pressure as in the pore scale problem. In Eq. (A13), a_{gl} is the liquid-gas interfacial area per unit volume

$$a_{gl} = \frac{A_{gl}}{V}. \tag{A14}$$

It is argued in (Whitaker, 2013) that the term $\nabla . (\boldsymbol{u} P_v^*)$ in Eq. (A13) is negligible. Thus, Eq. (A13) can be expressed as

$$\varepsilon \frac{\partial (1-S) P_v}{\partial t} = \nabla . \left(\varepsilon(1-S) D_{eff} \nabla P_v\right) + a_{gl} k (P_{sat} - P_v). \tag{A15}$$

It is important to note that the effective diffusivity D_{eff} is computed assuming zero flux on the liquid-gas interface. Also, note that the HKS theory was introduced for convenience in order to start from a formulation analogous to the one considered in (Whitaker, 2013). It is to be noted that the HKS theory is not included in the PNM drying algorithm.

For the characterization of liquid phase, we begin with the pore-scale expression

$$\frac{\partial \rho_l}{\partial t} = \nabla . (\rho_l \mathbf{v}). \tag{A16}$$

Applying the volume averaging method leads to

$$\varepsilon \rho_l \frac{\partial S}{\partial t} = \nabla . \langle \rho_l \mathbf{v} \rangle + \frac{1}{V} \int_{A_{lg}} \rho_l (\mathbf{v} - \mathbf{w}) . \mathbf{n}_{lg} dA, \tag{A17}$$

where $\mathbf{v}$ is the liquid phase mass average velocity and $\mathbf{w}$ is the velocity of liquid-gas interface. At a meniscus, we have

$$\rho_l (\mathbf{v} - \mathbf{w}) . \mathbf{n}_{lg} = \rho_v (\mathbf{v}_v - \mathbf{w}) . \mathbf{n}_{lg}, \tag{A18}$$

where $\mathbf{v}_v$ is the velocity of the water vapor and

$$\rho_v(\mathbf{v_v} - \mathbf{w}).\mathbf{n}_{lg} \approx -\frac{\widetilde{M}_v}{\tilde{R}T} D\nabla P_v.\mathbf{n}_{gl}. \tag{A19}$$

Assuming isolated liquid clusters and considering Eq. (A7), the convective liquid flow can be neglected, enabling us to express Eq. (A17) as

$$\varepsilon\rho_l \frac{\partial S}{\partial t} \approx -\frac{A_{gl}}{V}\frac{\widetilde{M}_v}{\tilde{R}T} k\big(P_{v,sat} - P_v\big). \tag{A20}$$

Taking into account Eq. (A14), we express Eq. (A20) as

$$\varepsilon\rho_l \frac{\partial S}{\partial t} \approx -a_{gl}\frac{\widetilde{M}_v}{\tilde{R}T} k\big(P_{v,sat} - P_v\big). \tag{A21}$$

The final form of the liquid and vapor phase equations of the two-equation CM for the limiting case of immobile liquid phase can thus be expressed as

$$\varepsilon\frac{\partial(1-S)P_v}{\partial t} = \nabla.\big(\varepsilon(1-S)D_{eff}\,\nabla P_v\big) + a_{gl}k\big(P_{v,sat} - P_v\big), \tag{A22}$$

$$\varepsilon\rho_l \frac{\partial S}{\partial t} \approx -a_{gl}\frac{\widetilde{M}_v}{\tilde{R}T} k\big(P_{v,sat} - P_v\big). \tag{A23}$$

References

Attari Moghaddam, A., Prat, M., Tsotsas, E., & Kharaghani, A. (2017). Evaporation in capillary porous media at the perfect piston-like invasion limit: Evidence of non-local equilibrium effects. Water Resources Research, 53(12), 10433–10449.

Bénet, J. C., & Jouanna, P. (1982). Phenomenological relation of phase change of water in a porous medium: Experimental verification and measurement of the phenomenological coefficient. International Journal of Heat and Mass Transfer, 25(11), 1747–175

Bénet, J.-C., Lozano, A.-L., Cherblanc, F., & Cousin, B. (2009). Phase change of water in a hygroscopic porous medium: Phenomenological relation and experimental analysis for water in soil. Journal of Non-Equilibrium Thermodynamics, 34(2), 133–153.

523 Blunt, M. J., Jackson, M. D., Piri, M., & Valvatne, P. H. (2001). Detailed physics, predictive
524 capabilities and upscaling for pore-scale models of multiphase flow. Advances in Water
525 Resources, 25, 1069–1089.

526 Culligan, K. A., Wildenschild, D., Christensen, B. S. B., Gray, W. G., & Rivers, M. L.
527 (2006). Pore-scale characteristics of multiphase flow in porous media: A comparison of air-
528 water and oil-water experiments. Advances in Water Resources, 29(2), 227–238.

529 Gomez, I., Sala, J. M., & Milln, J. A. (2007). Characterization of moisture transport
530 properties for lightened clay brick: Comparison between two manufacturers. Journal of
531 Building Physics, 31(2), 179–194.

532 Hassanizadeh, S. M., & Gray, W. G. (1990). Mechanics and thermodynamics of multiphase
533 flow in porous media including interphase boundaries. Advances in Water Resources, 13(4),
534 169–186.

535 Hassanizadeh, S. M., & Gray, W. G. (1993). Thermodynamic basis of capillary pressure in
536 porous media. Water Resources Research, 29(10), 3389–3405.

537 Joekar-Niasar, V., Hassanizadeh, S. M., & Leijnse, A. (2008). Insights into the relationships
538 among capillary pressure, saturation, interfacial area and relative permeability using pore-
539 network modeling. Transport in Porous Media, 74(2), 201–219.

540 Joekar-Niasar, V., Hassanizadeh, S. M., & Dahle, H. K. (2010). Non-equilibrium effects in
541 capillarity and interfacial area in two-phase flow: Dynamic pore-network modelling. Journal
542 of Fluid Mechanics, 655, 38–71.

543 Le Bray, Y., & Prat, M. (1999). Three-dimensional pore network simulation of drying in
544 capillary porous media. International Journal of Heat and Mass Transfer, 42(22), 4207–4224.

545 Li, Z., Vanderborght, J., & Smits, K. M. (2019). Evaluation of model concepts to describe
546 water transport in shallow subsurface soil and across the soil–air interface. Transport in
547 Porous Media, 128(3), 945–976.

548 Lockington, D. A., Parlange, J. Y., Barry, D. A., & Leech, C. A. (2003). Drying of porous
549 building materials: Hydraulic diffusivity and front propagation. Materials and
550 Structures/Materiaux et Constructions, 36(261), 448–452.

551 Marchand, R. G., & Kumaran, M. K. (1994). Moisture diffusivity of cellulose insulation.
552 Journal of Thermal Insulation and Building Envelops, 17, 362–377.

553 Metzger, T., Irawan, A., & Tsotsas, E. (2006). Erratum: Extension of Hoshen-Kopelman
554 algorithm to non-lattice environments (Physica A: Statistical Mechanics and Its Applications
555 (2003) 321 (665-678)). Physica A: Statistical Mechanics and Its Applications, 363(2), 558–
556 560.

557 Metzger, T., Irawan, A., & Tsotsas, E. (2007). Influence of pore structure on drying kinetics:
558 A pore network study. AIChE Journal, 53(12), 3029–3041.

559 Nowicki, S. C., Davis, H. T., & Scriven, L. E. (1992). Microscopic determination of transport
560 parameters in drying porous media. Drying Technology, 10(4), 925–946.

561 Øren, P. E., Bakke, S., & Arntzen, O. J. (1998). Extending predictive capabilities to network
562 models. SPE Journal, 3(4), 324–335.

563 Ouedraogo, F., Cherblanc, F., Naon, B., & Bénet, J. C. (2013). Water transfer in soil at low
564 water content: Is the local equilibrium assumption still appropriate? Journal of Hydrology,
565 492, 117–127.

566 Pel, L., Brocken, H., & Kopinga, K. (1996). Determination of moisture diffusivity in porous
567 media using moisture concentration profiles. International Journal of Heat and Mass Transfer,
568 39(6), 1273–1280.

569 Pel, L., Landman, K. A., & Kaasschieter, E. F. (2002). Analytic solution for the non-linear
570 drying problem. International Journal of Heat and Mass Transfer, 45, 3173–3180.

571 Philip, J. R., & De Vries, D. A. (1957). Moisture movement in porous materials under
572 temperature gradients. Transactions of American Geophysical Union, 38(2), 222.

573 Plumb, O., Gu, L., & Webb, S. W. (1999). Drying of porous materials at low moisture
574 content. Drying Technology, 17(10), 1999–2011.

575 Prat, M. (2002). Recent advances in pore-scale models for drying of porous media. Chemical
576 Engineering Journal, 86(1–2), 153–164.

577 Prat, M. (2011). Pore network models of drying, contact angle, and film flows. Chemical
578 Engineering & Technology, 34(7), 1029–1038.

579 Pujol, A., Debenest, G., Pommier, S., Quintard, M., & Chenu, D. (2011). Modeling
580 composting processes with local equilibrium and local non-equilibrium approaches for water
581 exchange terms. Drying Technology, 29(16), 1941–1953.

582 Schrage, R. W. (1953). A Theoretical Study of Interphase Mass Transfer. Columbia Univ.
583 Press, New York.

584 Schoeber, W. J. A. (1976). Regular regimes in sorption processes: Calculation of drying rates
585 and determination of concentration dependent diffusion coefficients (PhD thesis). Eindhoven,
586 The Netherlands: Technical University.

587 van Brakel, J. (1980). Mass transfer in convective drying. In Mujumdar, A. S. (ed.),
588 Advances in Drying, pp. 217–267. Hemisphere, New York.

589 Vorhauer, N., Metzger, T., & Tsotsas, E. (2010). Empirical macroscopic model for drying of
590 porous media based on pore networks and scaling theory. Drying Technology, 28(8), 991–
591 1000.

592 Wang, J. P., Lambert, P., De Kock, T., Cnudde, V., & François, B. (2019). Investigation of
593 the effect of specific interfacial area on strength of unsaturated granular materials by X-ray
594 tomography. Acta Geotechnica, 14, 1545–1559.

595 Whitaker, S. (2013). The Method of Volume Averaging. Springer Science & Business Media.

596 Whitaker, S. (1977). Simultaneous heat, mass, and momentum transfer in porous media: A
597 theory of drying. Advances in Heat Transfer, 13, 119–203.

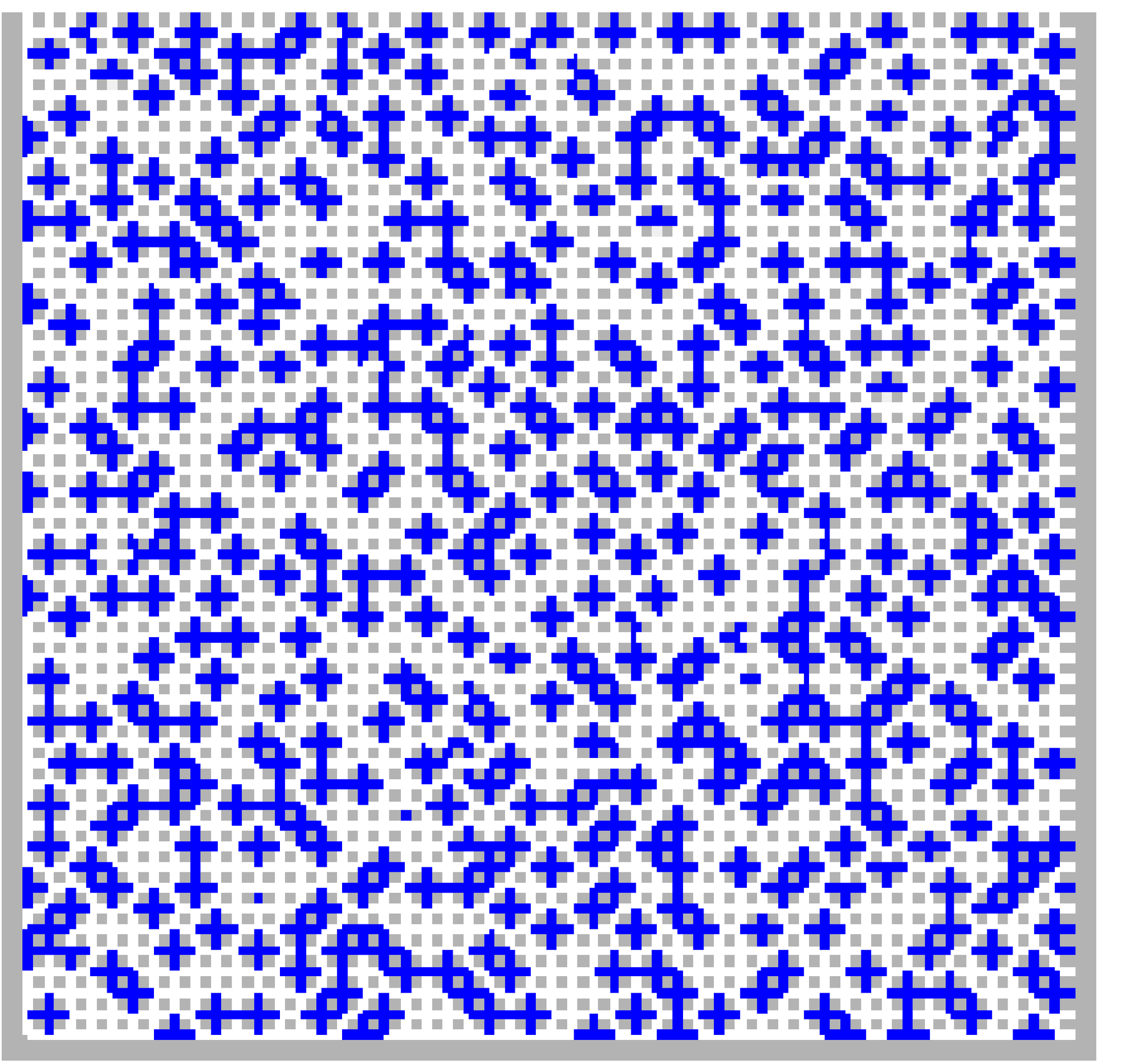

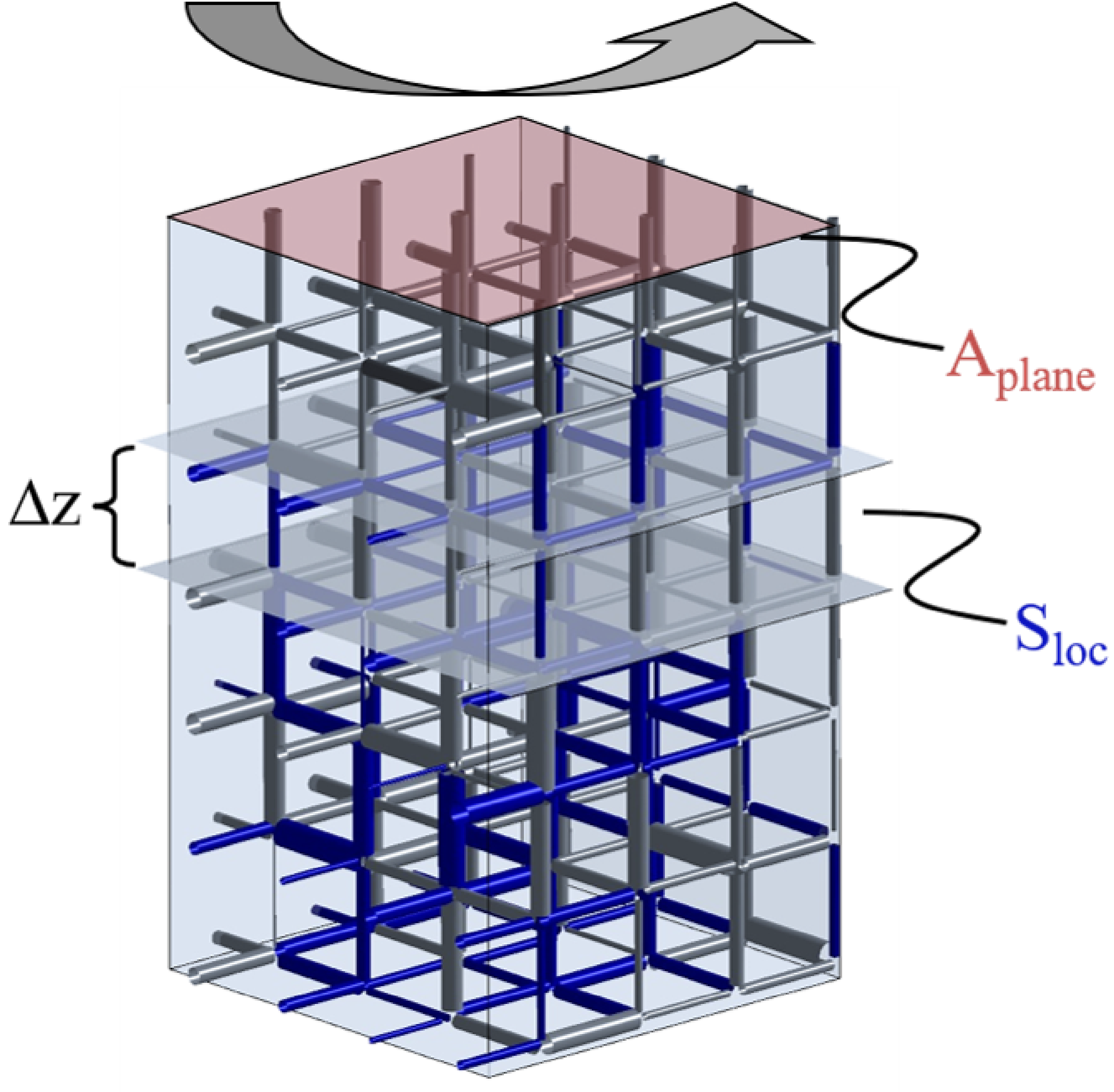
A_{plane}
Δz
S_{loc}

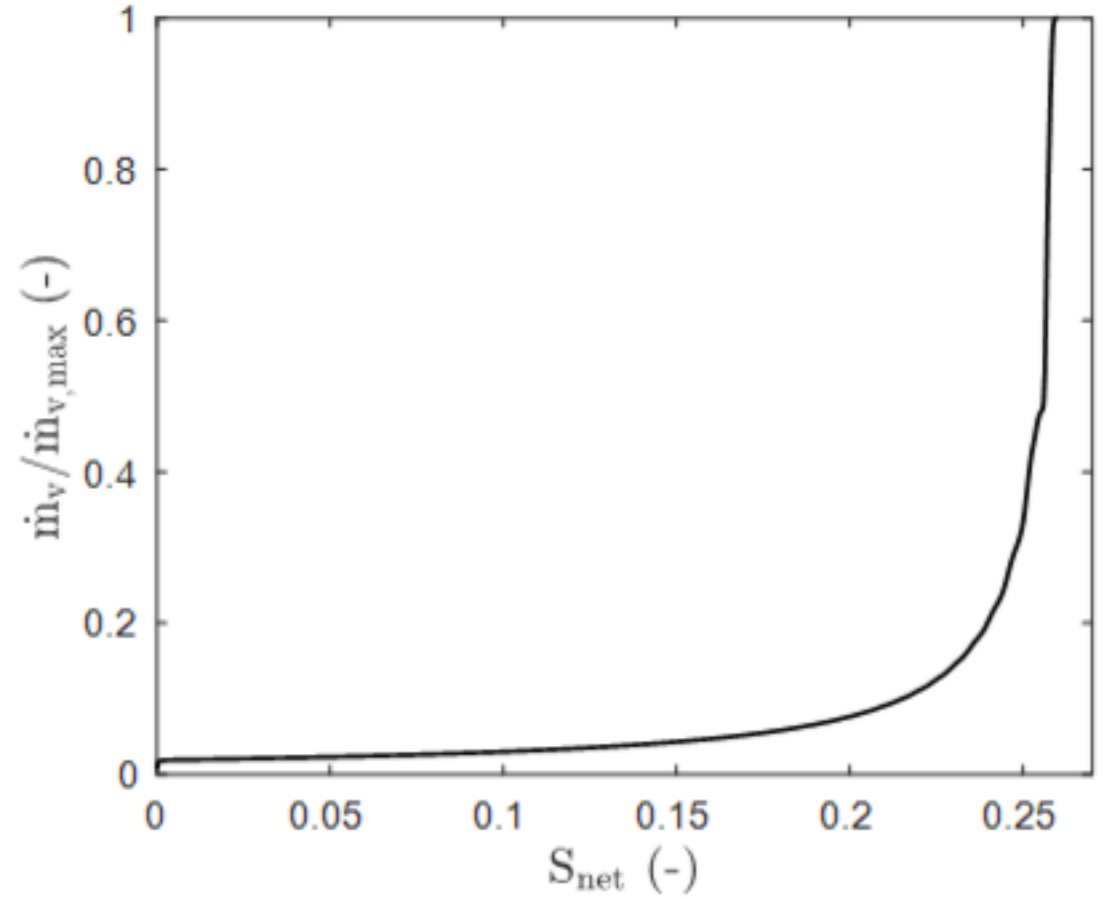
1
0.8
0.6
0.4
0.2
0
$\dot{m}_v/\dot{m}_{v,max}$ (-)
0
0.05
0.1
0.15
0.2
0.25
S_{net} (-)

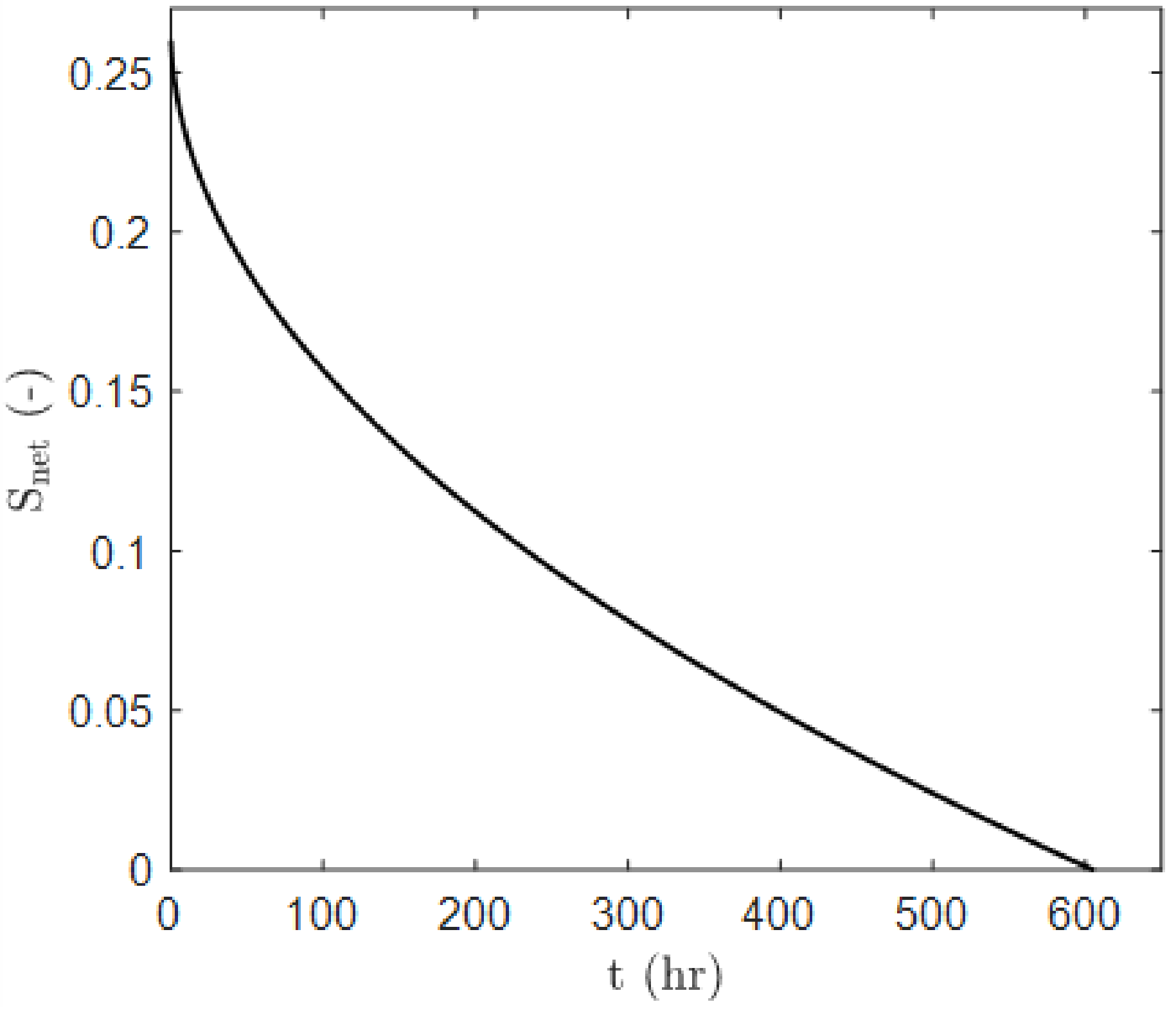
0.25
0.2
0.15
0.1
0.05
0
S_{net} (-)
0
100
200
300
400
500
600
t (hr)

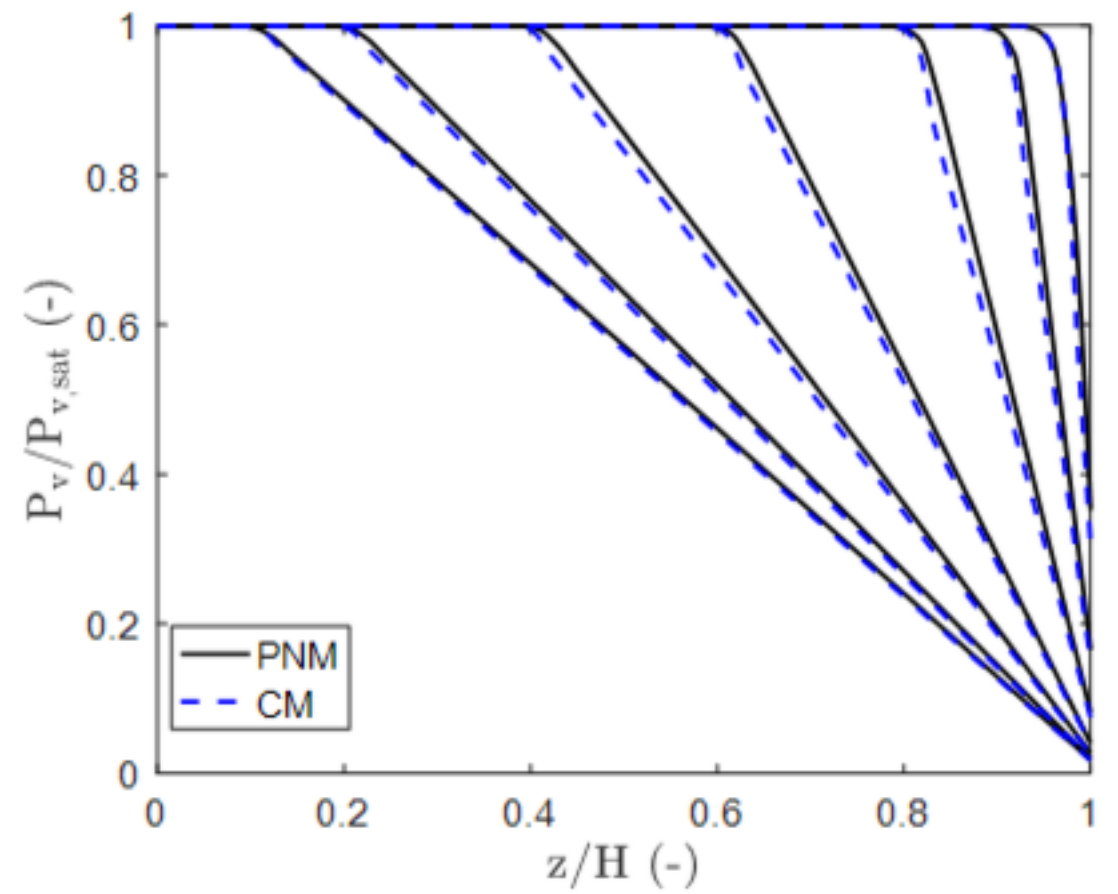
1
0.8
0.6
0.4
0.2
0
$P_v/P_{v,sat}$ (-)
PNM
CM
0
0.2
0.4
0.6
0.8
1
z/H (-)

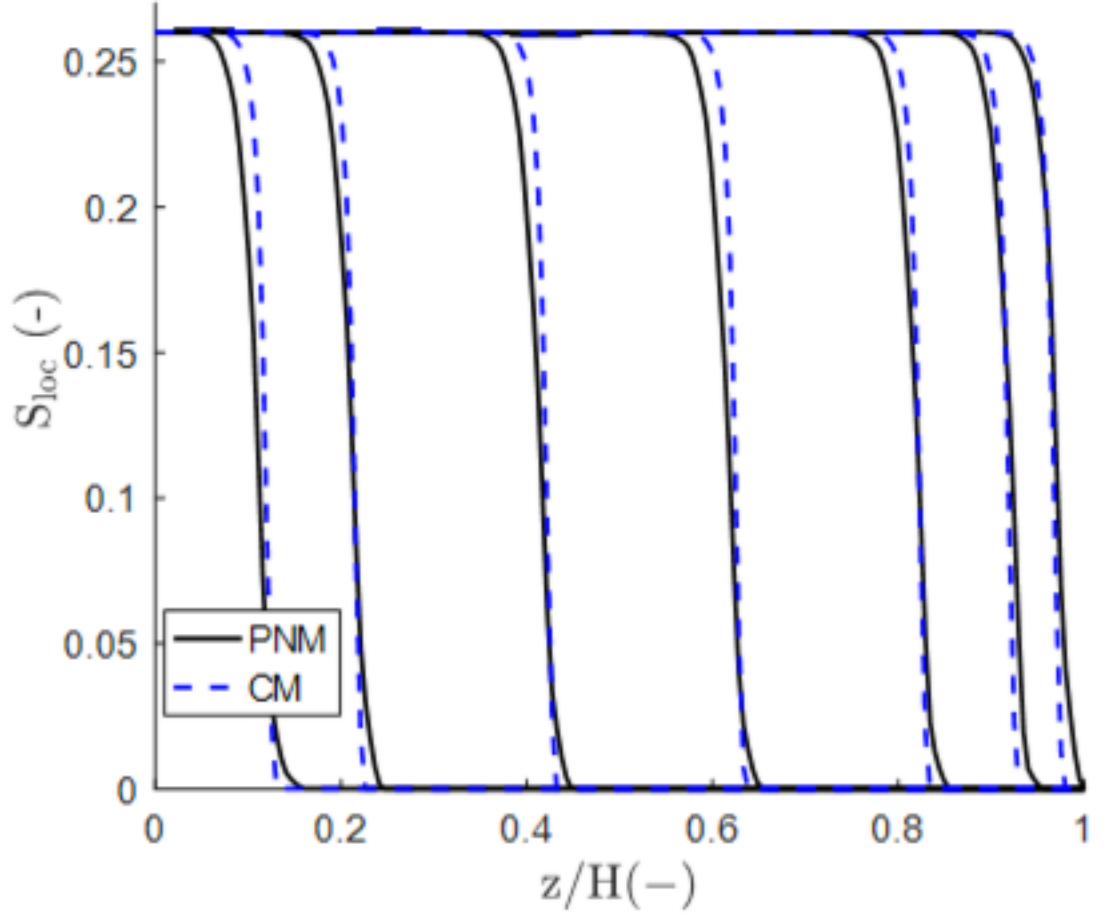
0.25
0.2
0.15
0.1
0.05
0
S_{loc} (-)
PNM
CM
0
0.2
0.4
0.6
0.8
1
z/H(−)

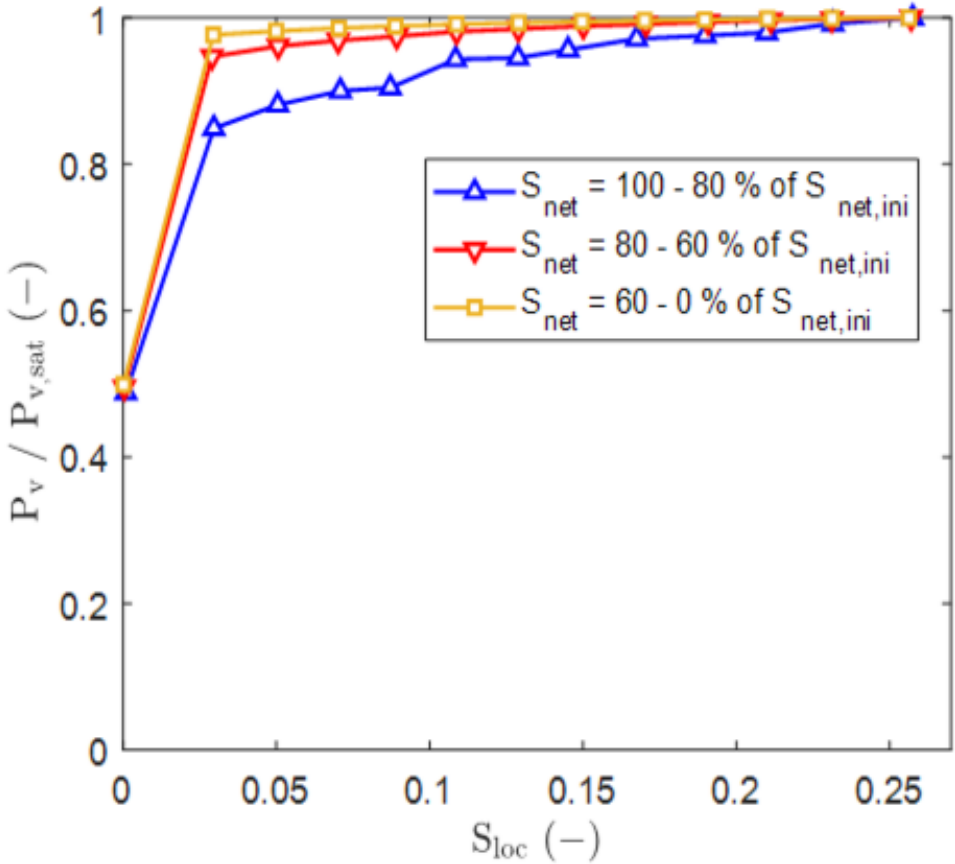
1
0.8
0.6
0.4
0.2
0
0
0.05
0.1
0.15
0.2
0.25
P_v / $P_{v,sat}$ (−)
S_{loc} (−)
S_{net} = 100 - 80 % of $S_{net,ini}$
S_{net} = 80 - 60 % of $S_{net,ini}$
S_{net} = 60 - 0 % of $S_{net,ini}$

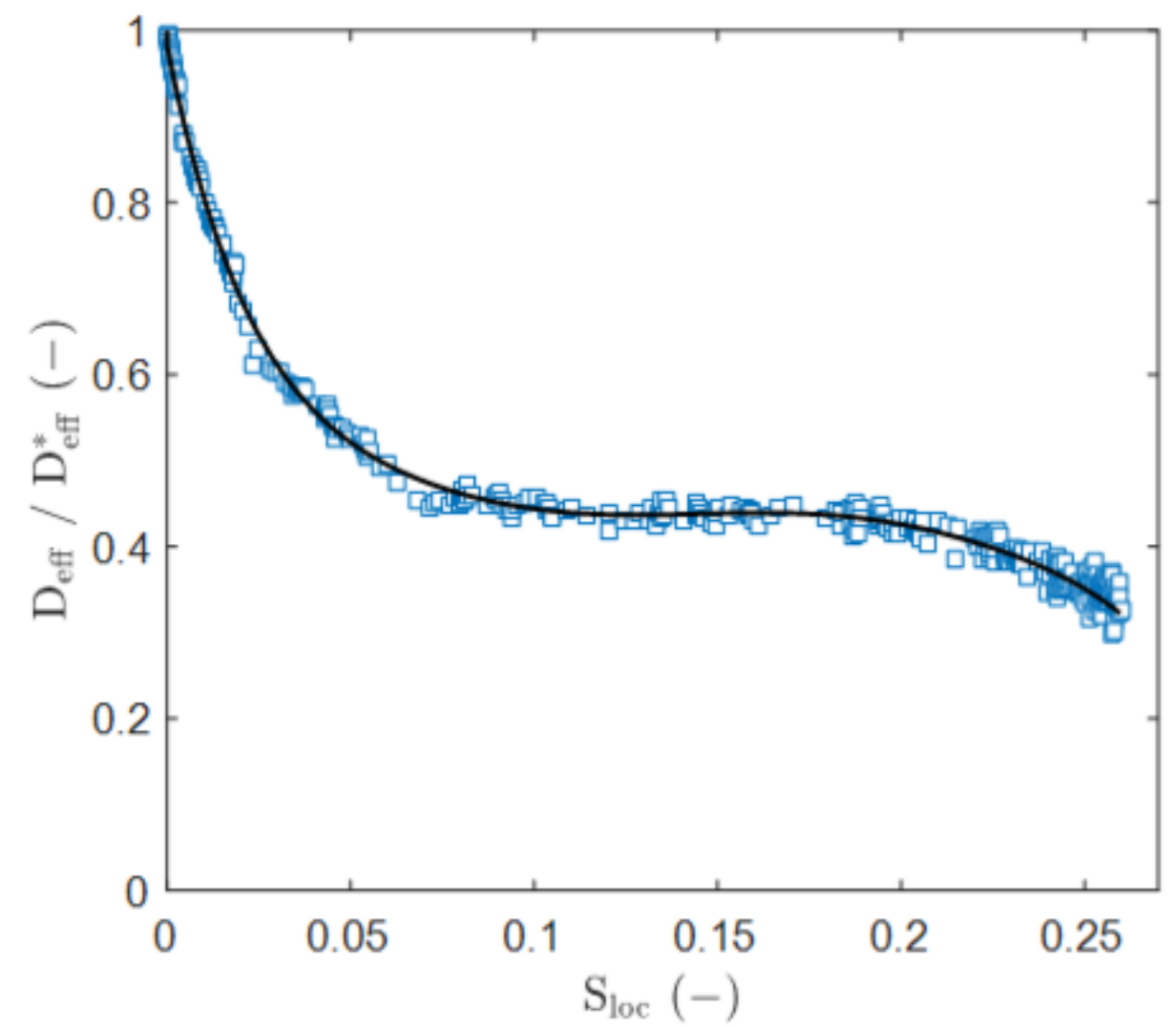
1
0.8
0.6
0.4
0.2
0
D_{eff} / D^*_{eff} (−)
0
0.05
0.1
0.15
0.2
0.25
S_{loc} (−)

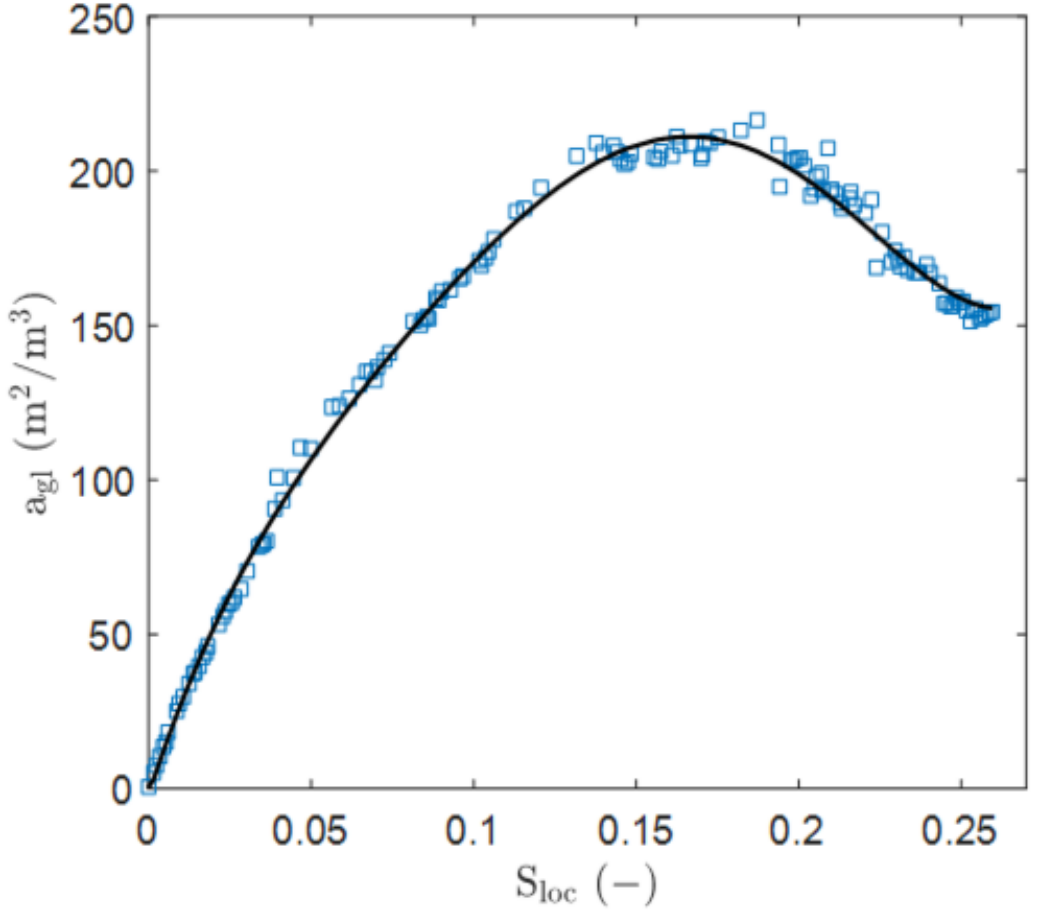
250
200
150
100
50
0
a_{gl} (m^2/m^3)
0
0.05
0.1
0.15
0.2
0.25
S_{loc} $(-)$

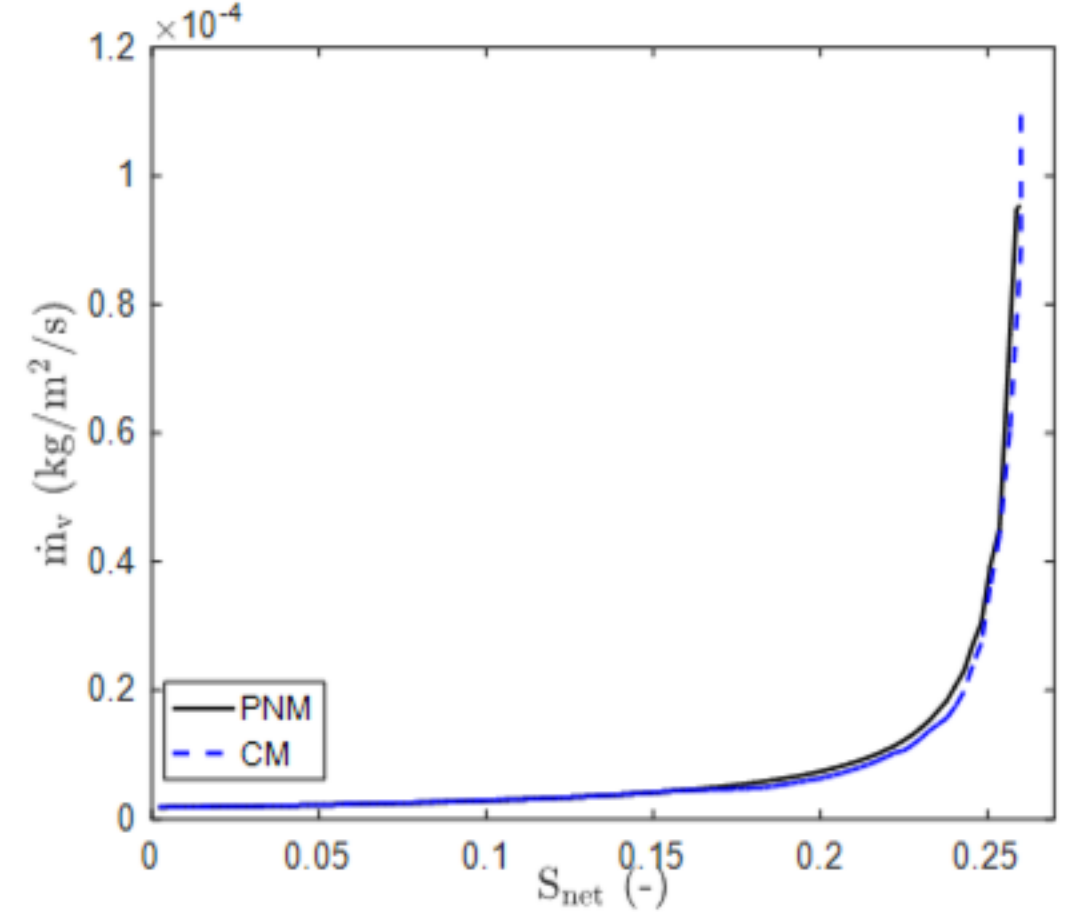
×10^-4
1.2
1
0.8
0.6
0.4
0.2
0
$\dot{m}_v$ (kg/m^2/s)
PNM
CM
0
0.05
0.1
0.15
0.2
0.25
S_{net} (-)

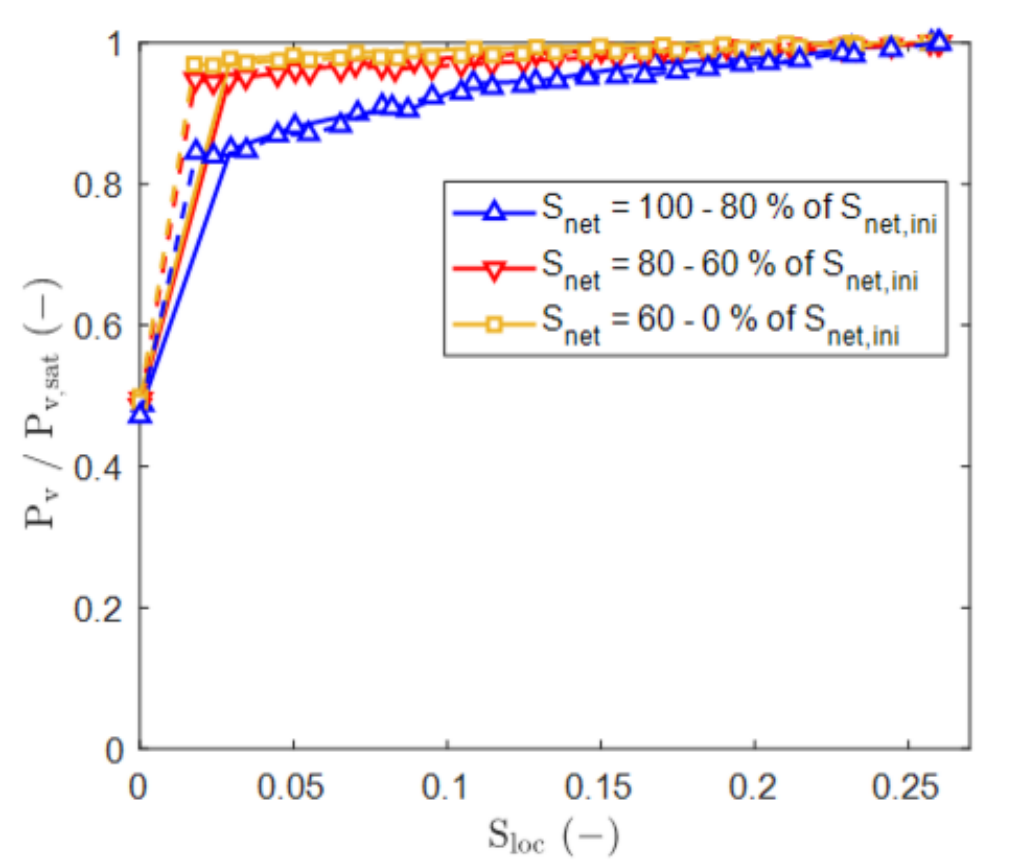
1
0.8
0.6
0.4
0.2
0
0
0.05
0.1
0.15
0.2
0.25
$P_v / P_{v,sat}$ (−)
S_{loc} (−)
S_{net} = 100 - 80 % of $S_{net,ini}$
S_{net} = 80 - 60 % of $S_{net,ini}$
S_{net} = 60 - 0 % of $S_{net,ini}$

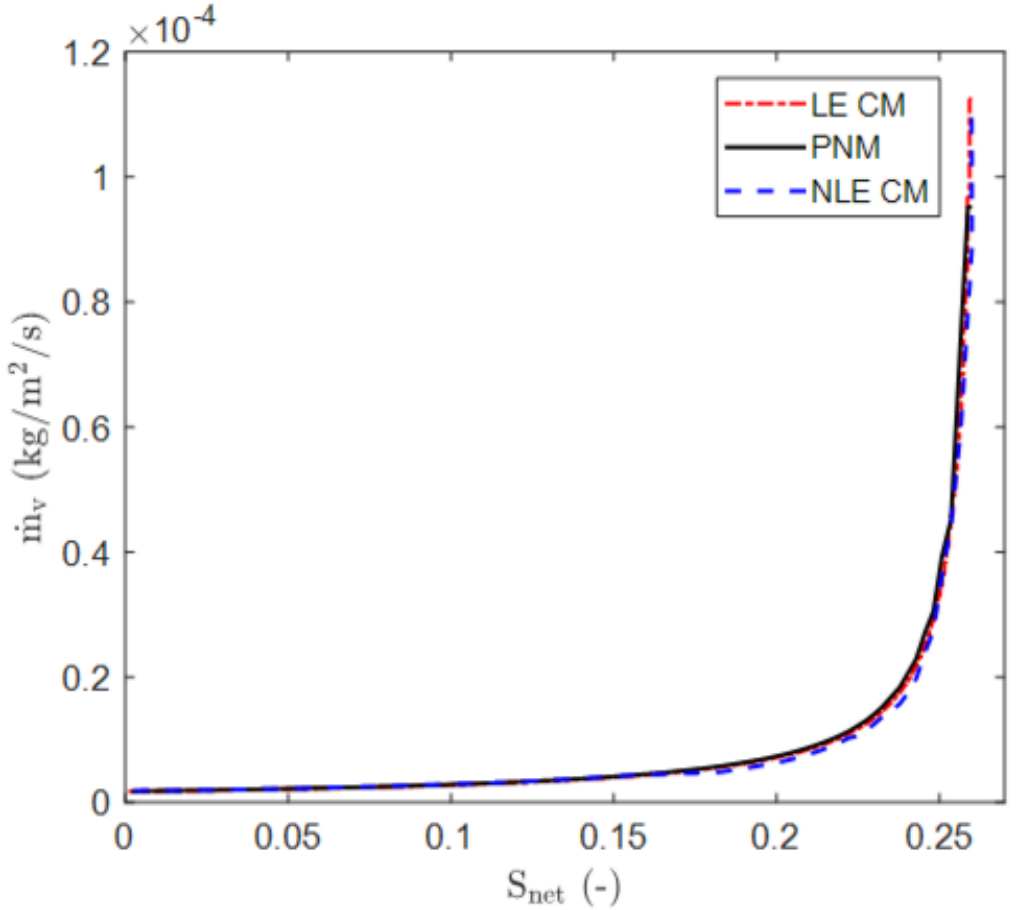
×10^-4
1.2
1
0.8
0.6
0.4
0.2
0
LE CM
PNM
NLE CM
$\dot{m}_v$ (kg/m^2/s)
0
0.05
0.1
0.15
0.2
0.25
S_{net} (-)

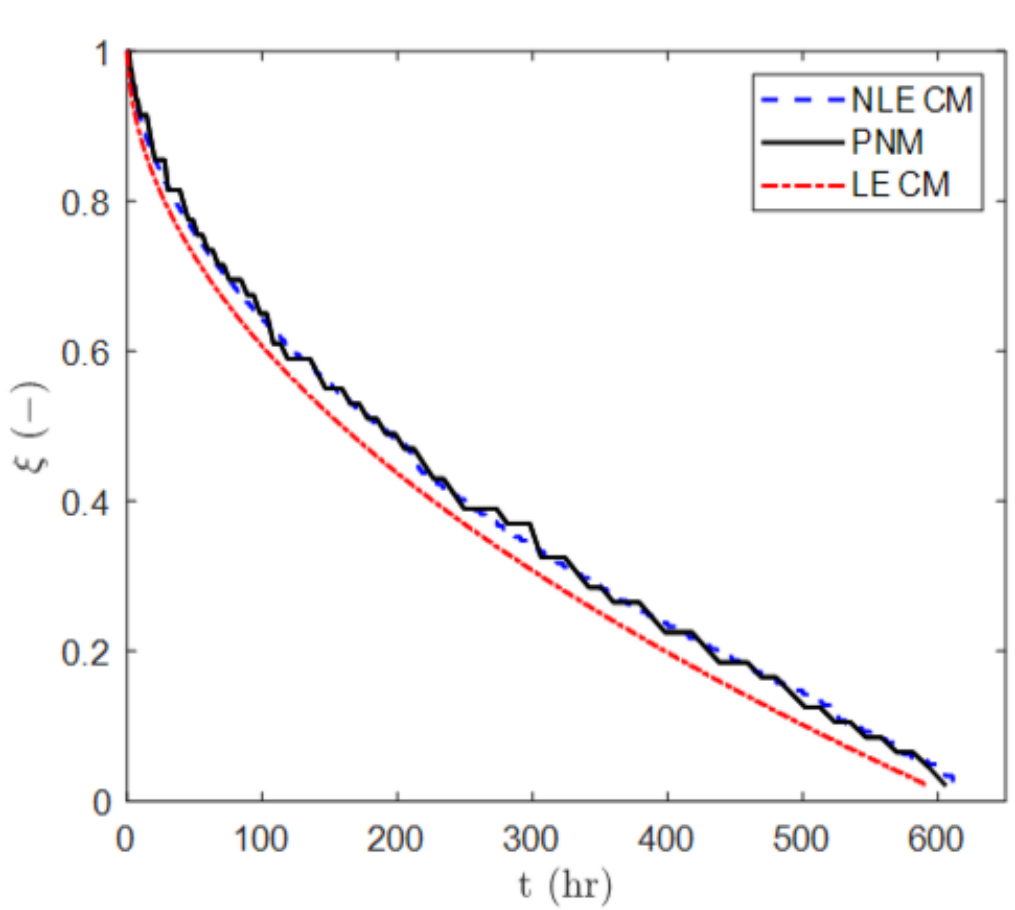
NLE CM
PNM
LE CM
ξ (−)
t (hr)
0
0.2
0.4
0.6
0.8
1
0
100
200
300
400
500
600

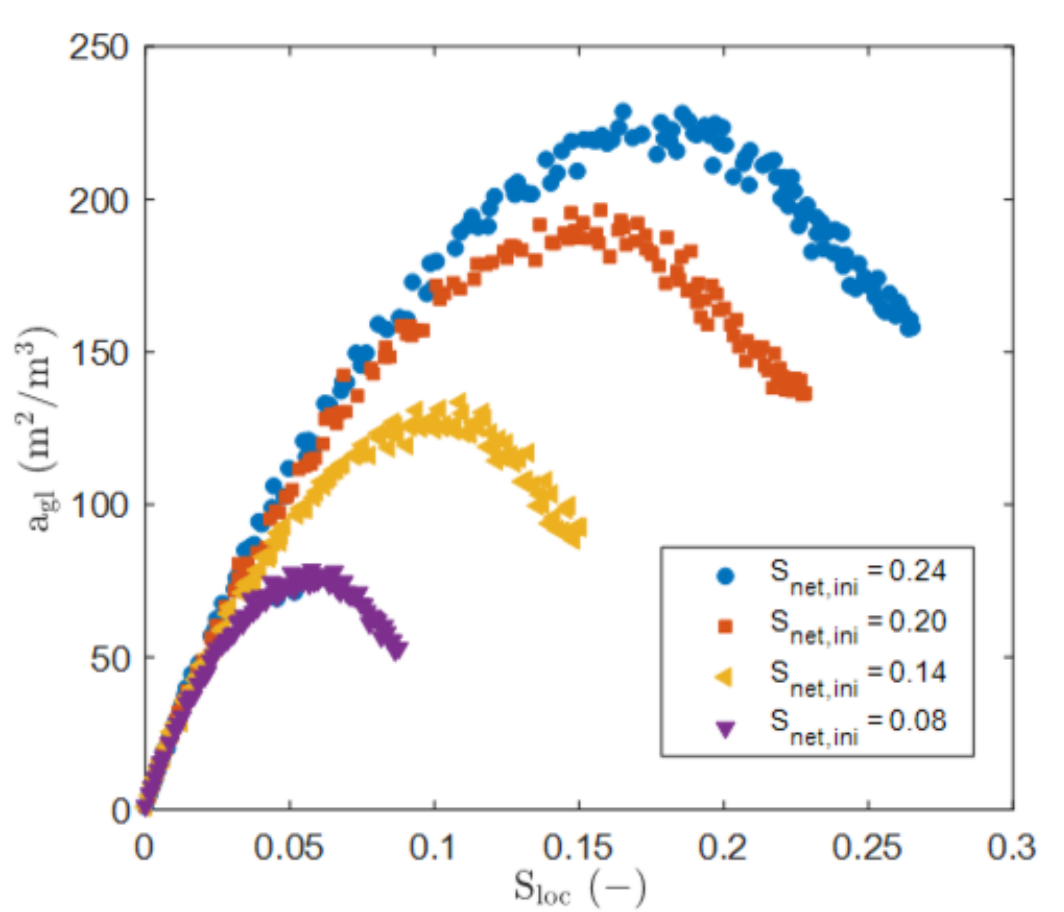
250
200
150
100
50
0
a_{gl} (m^2/m^3)
0
0.05
0.1
0.15
0.2
0.25
0.3
S_{loc} $(-)$
$S_{net,ini} = 0.24$
$S_{net,ini} = 0.20$
$S_{net,ini} = 0.14$
$S_{net,ini} = 0.08$

Structural property	**Unit**	**Value**	**Physical constant**	**Unit**	**Value**
Network size (nodes)	-	25×25×50	Temperature	K	293.15
Boundary layer discretization	-	25×25×4	Total gas pressure	Pa	10^5
Mean throat radius	μm	250	Diffusion coefficient	m^2/s	2.56×10^{-5}
Standard deviation of throat radius	μm	25	Saturation vapor pressure	Pa	2339
Throat length	mm	1	Surface tension	N/m	0.07274
Network porosity	-	0.594			